IMAGE RECOVERY METHODS FOR FREE-FLYING SYNTHETIC APERTURE RADIOMETERS

Matas Gelžinis
University of Southampton
Southampton, SO17 1BJ, UK
mg2n18@soton.ac.uk

Alexander Wittig
University of Southampton
Southampton, SO17 1BJ, UK
a.wittig@soton.ac.uk

***Abstract*—Free-flying distributed synthetic aperture radiometers can improve L-band imaging resolution, but formation perturbations introduce non-uniform (u, v) sampling that degrades conventional Fourier-sum inversion. We benchmark four reconstruction methods on a common test case: a six-satellite Golay6 formation at 250 km altitude with random in-plane displacements ($\sim$6.4 cm) and rotations (up to 5°). Using identical visibility inputs, we compare the Discrete Sum Method (DSM), a Voronoi-weighted DSM (VDSM), the Triangle Interpolation Method (TIM), and a reference NUFFT approach. DSM fails under the perturbed sampling, while VDSM, TIM, and NUFFT recover the main scene structure. RMS error shows TIM performs best near the image centre (8.54 K at 40° FOV radius), whereas NUFFT/VDSM are slightly better at the widest field ($\sim$16–18 K at 60°). Overall, methods that account for non-uniform sampling substantially improve robustness to formation drift.**

***Index Terms*—Synthetic aperture radiometry, non-uniform sampling, image reconstruction, formation flying.**

I. Introduction

Surface soil moisture and sea surface salinity are key state variables in the land–atmosphere system. They regulate evaporation, precipitation, and runoff, and therefore underpin applications ranging from flood forecasting to climate monitoring [1–3]. L-band microwave radiometry (1.4 GHz) provides strong sensitivity to these parameters because of its comparatively deep soil penetration and reduced sensitivity to surface roughness [4–6]. The principal limitation is spatial resolution: diffraction requires apertures that are prohibitively large for conventional single-dish instruments [7]. Synthetic aperture radiometry addresses this by correlating signals from multiple small antennas to synthesize a larger effective aperture, as demonstrated by SMOS [8–10]. However, SMOS resolution (on the order of 50 km) remains insufficient for many geophysical applications that require sub-10 km detail [8–10].

Distributed formations of small satellites offer a scalable route to higher resolution by enabling longer baselines of the spatial-frequency (uv) plane [11–13]. In practice, image quality depends not only on uv coverage but also on the fidelity of the assumed baseline geometry. Conventional inversion approaches based on discrete Fourier summation are sensitive to baseline perturbations, leading to rapid degradation when spacecraft drift from nominal positions [12, 13]. This sensitivity drives stringent formation-keeping requirements; for example, the TriHex mission concept limits relative offsets to 5 mm [12]. More robust reconstruction algorithms could relax these constraints, improving mission feasibility and scalability.

In this study, we compare four image reconstruction methods - a baseline approach, two methods developed in this work, and a reference method from the literature - and quantify their ability to recover surface brightness temperature maps under formation-induced non-uniform uv sampling.

II. Methodology

We consider a distributed L-band synthetic aperture radiometer formed by six small satellites in a Golay6 configuration at an altitude of 250 km [14]. No active formation control is assumed and each spacecraft is displaced from its nominal position in the formation plane and subjected to a small rigid-body rotation. Figure 1 illustrates one representative case, in which the six satellites are translated by approximately 6.4 cm (in random in-plane directions) and rotated by up to 5° about their centres.

From the perturbed antenna phase-centre locations, we form all pairwise baselines and express them as spatial frequencies in the (u, v) plane by normalising by the wavelength. The resulting (u, v) samples for the case in Fig. 1 are shown in Fig. 2, with colour indicating baseline redundancy. The perturbations break the ideal lattice structure: the sampling becomes non-uniform, with mis-registered tiles, local gaps, and intra-tile distortions. Note that for visualisation and for the two discrete-sum methods, we merge near-coincident baselines in the (u, v) plane using a distance threshold of half the nominal lattice spacing.

To benchmark reconstruction performance, we use the brightness temperature scene shown in Fig. 3. The map is adapted from [15] and rendered as viewed from 250 km above 35°N, 90°W over a 60° field of view. Values are scaled to a representative L-band brightness temperature range, and the image grid is parameterised by direction cosines (ξ, η). Reconstruction accuracy is evaluated for four methods: the standard Discrete Sum Method (DSM), a Voronoi-weighted

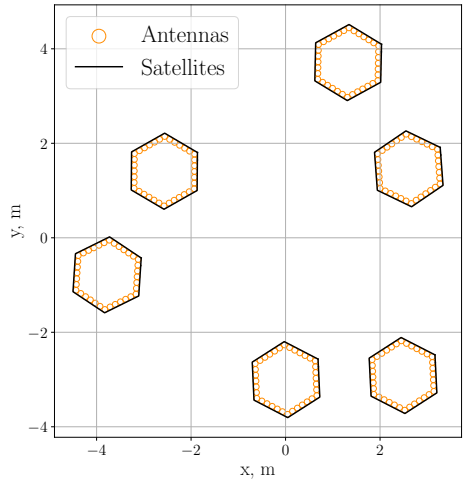

Fig. 1: A Golay6 formation [14]. Note that the satellites are slightly displaced and rotated.

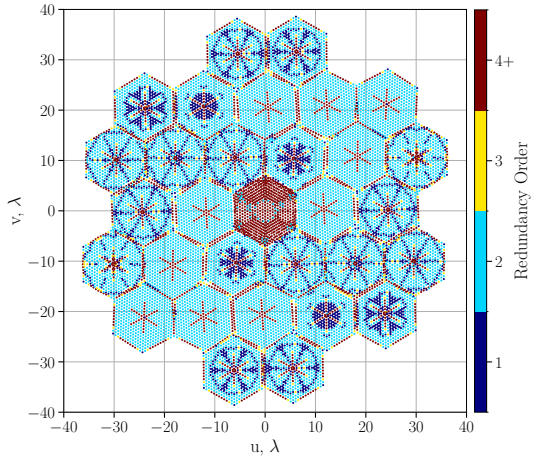

Fig. 2: Baselines of the antenna arrangement from Fig. 1. Point colour signifies redundancy.

Discrete Sum Method (VDSM), the Triangle Interpolation Method (TIM), and a reference non-uniform Fourier transform approach from Fessler and Sutton [16].

A. Discrete Sum Method

Under the standard assumptions used in synthetic aperture radiometry (narrowband measurement, far-field scene, and a small-angle parametrisation by direction cosines), the brightness temperature map $T_B(\xi,\eta)$ is related to the measured complex visibility function $\mathcal{V}(u,v)$ through a two-dimensional inverse Fourier transform [17]:

$$T_B(\xi,\eta) = \iint_{-\infty}^{\infty} \mathcal{V}(u,v)\, e^{2\pi j(u\xi+v\eta)}\, du\, dv. \tag{1}$$

DSM approximates (1) by replacing the continuous integral with a finite weighted sum over N measured visibilities

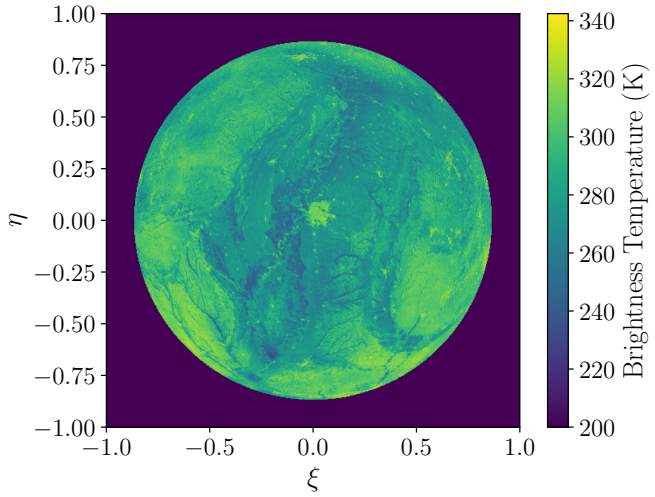

Fig. 3: Input image adapted from [15].

$\{\mathcal{V}_i\}_{i=1}^{N}$ at baseline coordinates $\{(u_i,v_i)\}_{i=1}^{N}$ [12, 13, 18, 19]:

$$T_B(\xi,\eta) = \sum_{i=1}^{N} \mathcal{V}_i\, W_i\, e^{2\pi j(u_i\xi+v_i\eta)}. \tag{2}$$

The weights W_i apply apodisation to mitigate sidelobes arising from the finite extent of the sampled spatial-frequency domain. In this work, a Hamming window is used throughout. A key assumption of DSM is that the (u,v) samples lie on a uniform lattice (or can be treated as such), so that (2) corresponds to an inverse discrete Fourier transform on a regular grid. Formation drift violates this assumption by perturbing baseline coordinates, which in turn produces non-uniform sampling and degrades the reconstruction. Consequently, DSM-based processing can impose stringent formation-keeping requirements in distributed architectures.

B. Voronoi Discrete Sum Method

VDSM compensates for non-uniform sampling by assigning each visibility measurement a weight proportional to the area of its associated Voronoi cell in the (u,v) plane. A Voronoi diagram partitions the plane into regions whose points are closer to a given sample location than to any other [20]; the resulting cell area provides an estimate of the local sampling density inverse.

Let A_i denote the Voronoi cell area associated with sample (u_i,v_i). VDSM reconstructs the image via

$$T_B(\xi,\eta) = \sum_{i=1}^{N} \mathcal{V}_i\, A_i\, W_i\, e^{2\pi j(u_i\xi+v_i\eta)}, \tag{3}$$

where W_i is the same apodisation window introduced before. Figure 4 illustrates the resulting weighting behaviour: samples adjacent to gaps receive larger A_i, while samples in locally dense clusters are down-weighted. Voronoi cells on the convex hull are formally unbounded; following common practice, these boundary cells are assigned a finite nominal area, taken

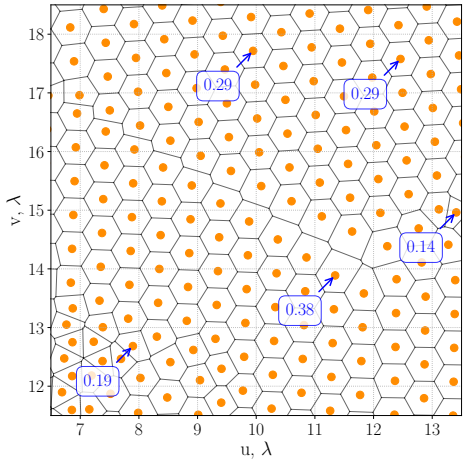

Fig. 4: Zoomed-in Voronoi diagram of the baseline arrangement from Fig. 2. Numbers in blue indicate cell area.

here to be the area of a regular hexagonal cell corresponding to the nominal lattice.

C. Triangle Interpolation Method

The Triangle Interpolation Method reconstructs the image by approximating the visibility function $\mathcal{V}(u,v)$ as piecewise linear over a Delaunay triangulation of the measured (u,v) samples. Specifically, the measured baseline locations are triangulated, $\mathcal{V}(u,v)$ is assumed to vary linearly within each triangle, and the inverse Fourier integral is evaluated analytically over each triangular element. The recovered brightness temperature map is then obtained as the sum of all triangle contributions.

Starting from (1), we restrict the integral to a single triangle and introduce barycentric coordinates (α,β) on the reference simplex. For vertex visibilities $\mathcal{V}_{1,2,3}$ at (u_i,v_i), the contribution of one triangle can be written as

$$T_{B\triangle}(\xi,\eta) = e^{kC}\, 2\mathcal{A}_\triangle \int_0^1 \int_0^{1-\alpha} \Big[\alpha\mathcal{V}_1 + \beta\mathcal{V}_2 + (1-\alpha-\beta)\mathcal{V}_3\Big]\, e^{k(\alpha A+\beta B)}\, d\beta\, d\alpha, \tag{4}$$

with

$$\begin{aligned} A &= \xi u_1 + \eta v_1 - (\xi u_3 + \eta v_3) \\ B &= \xi u_2 + \eta v_2 - (\xi u_3 + \eta v_3)) \\ C &= \xi u_3 + \eta v_3 \\ k &= 2j\pi \end{aligned} \tag{5}$$

where $\mathcal{A}_\triangle$ is the triangle area arising from the Jacobian of the change of variables. The double integral of (4) has a closed form, which can be shown to be:

$$I_\triangle = \frac{\begin{aligned} &A^2 \mathrm{e}^{kB}\Big[B(\mathcal{V}_1+\mathcal{V}_3-\mathcal{V}_2(Ak+2)) + A(\mathcal{V}_2-\mathcal{V}_3) + B^2k\mathcal{V}_2\Big] \\ &+ B^2\mathrm{e}^{kA}\Big[A^2k\mathcal{V}_1 + A(\mathcal{V}_2+\mathcal{V}_3-\mathcal{V}_1(Bk+2)) + B(\mathcal{V}_1-\mathcal{V}_3)\Big] \\ &- (A-B)^2\Big[A\mathcal{V}_2 + B\mathcal{V}_1 - \mathcal{V}_3(ABk+A+B)\Big] \end{aligned}}{A^2B^2k^3(A-B)^2}, \tag{6}$$

so that the full image is the sum of N triangle contributions,

$$T_B(\xi,\eta) = \sum_{i=1}^{N} e^{2j\pi C_i} 2\mathcal{A}_{\triangle i} I_{\triangle i}. \tag{7}$$

a) Numerical evaluation.: Although (6) is written with denominators that vanish at $A=0$, $B=0$, or $A=B$, the limit of the fraction is finite. In practice, stable evaluation is obtained by switching to the corresponding limiting expressions, which can be found using L'Hôpital's rule, whenever $|A|$, $|B|$, or $|A-B|$ falls below a small tolerance. In our implementation, a threshold on the order of 10^{-4} was sufficient.

b) Interpolation transfer function correction.: Because TIM models $\mathcal{V}(u,v)$ as piecewise linear, it implicitly applies a compact interpolation kernel in the (u,v) domain. On an ideal regular hexagonal lattice, this is equivalent to convolving the sampled visibilities with a hexagonal tent kernel. By the convolution theorem, this produces a known apodisation in the reconstructed $T_B(\xi,\eta)$ equal to the Fourier transform of the interpolation kernel, a sinc^3 window. We therefore apply a final scaling (deapodisation) by dividing the reconstructed image by this transfer function to correct the interpolation-induced attenuation, particularly towards the field-of-view edges.

D. Non-uniform Fourier transform

As a reference for comparison with TIM, we use the non-uniform fast Fourier transform (NUFFT) of Fessler and Sutton [16], which has previously been applied to synthetic aperture radiometry with intentionally non-uniform antenna layouts [21]. We use the `PyNUFFT` implementation [22]. In this approach, the irregular (u,v) samples are first gridded onto an oversampled Cartesian lattice using a compact interpolation kernel, a standard FFT is applied, and a final deapodisation is used to correct for the gridding kernel.

III. Results

Reconstructions of the same input scene using the four methods are shown in Fig. 5. DSM performs poorly under the perturbed, non-uniform (u,v) sampling: the reconstruction is strongly blurred and fine-scale structure is largely lost. In contrast, PyNUFFT, TIM, and VDSM recover the main spatial patterns, although residual blur and sampling-induced artefacts (notably ripples) remain visible.

Quantitative performance is summarised by the RMS error in Tab. I as a function of field-of-view (FoV) radius. TIM achieves the lowest error for smaller FoVs (i.e., near the scene centre). As the FoV increases and edge regions are included, the TIM error increases and becomes comparable to, or slightly worse than, PyNUFFT and VDSM at the largest radius, indicating reduced robustness near the FoV boundary for this test case.

IV. Conclusions

This work compared four reconstruction approaches for a free-flying distributed L-band synthetic aperture radiometer

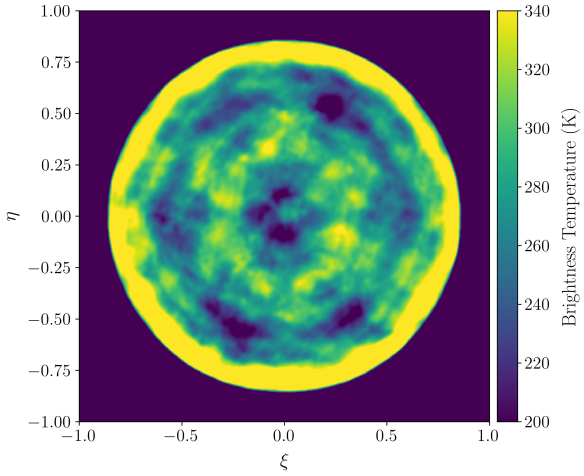

(a) DSM

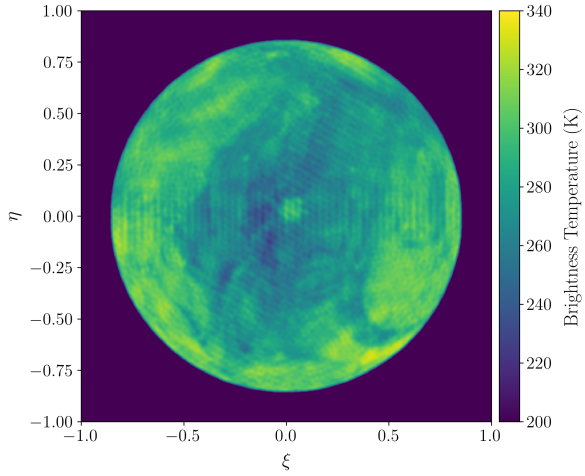

(b) VDSM

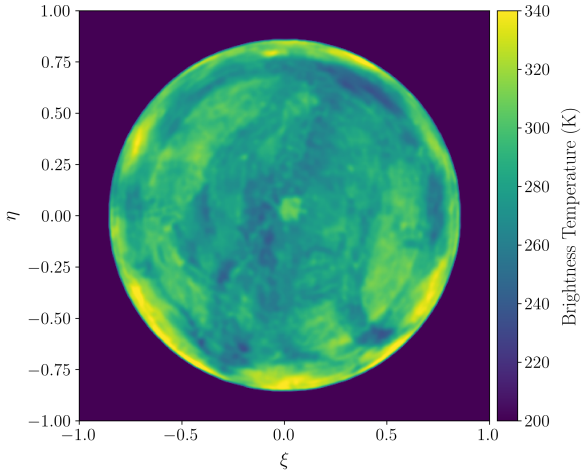

(c) TIM

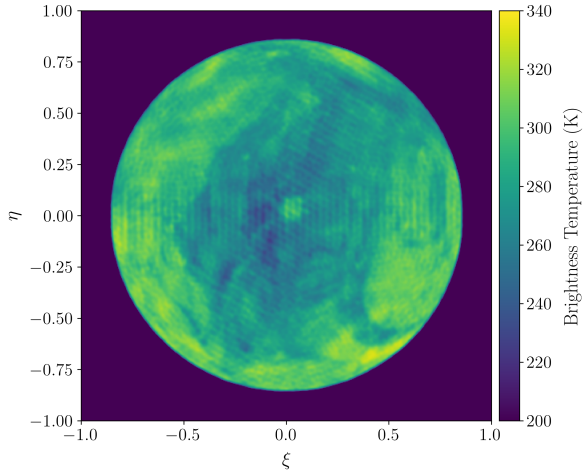

(d) PyNUFFT

Fig. 5: Reconstructed brightness temperature maps for four reconstruction methods.

TABLE I: Reconstruction error as a function of field-of-view radius for the displaced Golay6 test case.

FoV radius (°)	DSM [K]	VDSM [K]	TIM [K]	PyNUFFT[K]
20	32.45	14.30	8.39	14.07
40	33.39	10.29	8.54	10.23
60	46.18	17.58	17.75	15.87

under non-uniform (u, v) sampling induced by formation perturbations. The baseline discrete sum method was found to be highly sensitive to sampling irregularity, producing substantial blur and losing fine-scale structure in the recovered brightness temperature map. In contrast, VDSM, TIM, and the NUFFT-based reconstruction all provided markedly improved image quality by explicitly accounting for non-uniform sampling, either through density compensation (VDSM), analytic integration over a triangulated (u, v) mesh (TIM), or gridding with deapodisation (NUFFT). Quantitatively, TIM achieved the lowest RMS error when evaluation was restricted to the inner field of view, while its error increased toward the scene boundary and became comparable to (or slightly worse than) VDSM and PyNUFFT at the largest FOV radius. Overall, the results indicate that robust non-uniform sampling methods can substantially mitigate drift-induced degradation and therefore have the potential to relax stringent formation-keeping requirements in future distributed synthetic aperture radiometer missions. Future work will extend the analysis across a wider range of more realistic perturbations.

REFERENCES

[1] M. Berger, A. Camps, J. Font, Y. Kerr, J. Miller, J. Johannessen, B. Jacqueline, M. Drinkwater, N. Skou, N. Floury, M. Rast, H. Rebhan, and E. Attema, "Measuring ocean salinity with esa's smos mission - advancing the science," *ESA bulletin. Bulletin ASE. European Space Agency*, vol. 111, 08 2002.

[2] A. Beljaars, P. Viterbo, M. Miller, and A. Betts, "The anomalous rainfall over the united states during july 1993: Sensitivity to land surface parameterization and soil moisture anomalies," *Monthly Weather Review*, vol. 124, pp. 362–383, 03 1996.

[3] P. A. Dirmeyer and K. L. Brubaker, "Contrasting evaporative moisture sources during the drought of 1988 and the flood of 1993," *JGR*, vol. 104, no. D16, pp. 19,383–19,397, Aug. 1999.

[4] T. J. Schmugge, "Effect of texture on microwave emission from soils," *IEEE Transactions on Geoscience and Remote Sensing*, vol. GE-18, no. 4, pp. 353–361, 1980.

[5] R. Lang, Y. Zhou, C. Utku, and D. Le Vine, "Accurate measurements of the dielectric constant of seawater at l band," *Radio Science*, vol. 51, no. 1, pp. 2–24, 2016.

[6] J. T. Johnson, K. C. Jezek, G. Macelloni, M. Brogioni, L. Tsang, E. P. Dinnat, J. P. Walker, N. Ye, S. Misra, J. R. Piepmeier, R. Bindlish, D. M. LeVine, P. E. O'Neill, L. Kaleschke, M. J. Andrews, C. Yardim, M. Aksoy, M. Durand, C.-C. Chen, O. Demir, A. Bringer, J. Z. Miller, S. T. Brown, R. Kwok, T. Lee, Y. Kerr, D. Entekhabi, J. Peng, A. Colliander, S. Chan, J. A. MacGregor, B. Medley, R. DeRoo, and M. Drinkwater, "Microwave radiometry at frequencies from 500 to 1400 mhz: An emerging technology for earth observations," *IEEE Journal of Selected Topics in Applied Earth Observations and Remote Sensing*, vol. 14, pp. 4894–4914, 2021.

[7] J. J. Condon and S. M. Ransom, *Essential Radio Astronomy*. Princeton University Press, 2016, ch. 1, pp. 1–19, online edition hosted by NRAO. [Online]. Available: https://www.cv.nrao.edu/~sransom/web/Ch1.html

[8] D. Le Vine, A. Griffis, C. Swift, and T. Jackson, "Estar: a synthetic aperture microwave radiometer for remote sensing applications," *Proceedings of the IEEE*, vol. 82, no. 12, pp. 1787–1801, 1994.

[9] Y. Kerr, D. De Castro, A. Zurita, and J. Closa, "Low Frequency Passive Microwave User Requirement Consolidation Study: Cluster Analysis Report," CESBIO, Tech. Rep. SO-TN-CB-GS-0082, Oct. 2019. [Online]. Available: https://hal.science/hal-04845270

[10] Y. H. Kerr, N. Rodriguez-Fernandez, E. Anterrieu, M.-J. Escorihuela, M. Drusch, J. Closa, A. Zurita, F. Cabot, T. Amiot, R. Bindlish, and P. O'Neill, "The next generation of l band radiometry: User's requirements and technical solutions," in *IGARSS 2020 - 2020 IEEE International Geoscience and Remote Sensing Symposium*, 2020, pp. 5974–5977.

[11] J.-M. Goutoule and F. De Boer, "Large interferometer antennas synthesised by satellites in formation for earth remote sensing," in *IGARSS 2000. IEEE 2000 International Geoscience and Remote Sensing Symposium. Proceedings (Cat. No.00CH37120)*, vol. 2, 2000, pp. 869–870 vol.2.

[12] M. Martín-Neira, F. Scala, A. M. Zurita, M. Suess, M. Piera, B. J. Duesmann, M. Drusch, C. Colombo, D. De Wilde, J. C. Soteras, E. Gandini, R. Díez-García, R. Oliva, and I. Corbella, "Trihex: Combining formation flying, general circular orbits, and alias-free imaging, for high-resolution l-band aperture synthesis," *IEEE Transactions on Geoscience and Remote Sensing*, vol. 61, pp. 1–17, 2023.

[13] A. Akins, A. Tanner, A. Colliander, N.-J. Schlegel, K. Boudad, I. Yanovsky, S. Brown, and S. Misra, "A sparse synthetic aperture radiometer constellation concept for remote sensing of antarctic ice sheet temperature," *IEEE Transactions on Geoscience and Remote Sensing*, vol. PP, pp. 1–1, 01 2025.

[14] M. Gelžinis and A. Wittig, "Non-redundant golay formations for high-resolution l-band aperture synthesis," *International Journal of Remote Sensing*, vol. 0, no. 0, pp. 1–13, 2025. [Online]. Available: https://doi.org/10.1080/01431161.2025.2603694

[15] N. Vergopolan, N. W. Chaney, M. Pan, J. Sheffield, H. E. Beck, C. R. Ferguson, L. Torres-Rojas, S. Sadri, and E. F. Wood, "Smap-hydroblocks, a 30-m satellite-based soil moisture dataset for the conterminous us," *Scientific Data*, vol. 8, no. 1, p. 264, 2021. [Online]. Available: https://www.nature.com/articles/s41597-021-01050-2

[16] J. Fessler and B. Sutton, "Nonuniform fast fourier transforms using min-max interpolation," *IEEE Transactions on Signal Processing*, vol. 51, no. 2, pp. 560–574, 2003.

[17] I. Corbella, N. Duffo, M. Vall-llossera, A. Camps, and F. Torres, "The visibility function in interferometric aperture synthesis radiometry," *IEEE Transactions on Geoscience and Remote Sensing*, vol. 42, no. 8, pp. 1677–1682, 2004.

[18] A. K. Sugihara El Maghraby, A. Grubišić, C. Colombo, and A. Tatnall, "A novel interferometric microwave radiometer concept using satellite formation flight for geostationary atmospheric sounding," *IEEE Transactions on Geoscience and Remote Sensing*, vol. 56, no. 6, pp. 3487–3498, 2018.

[19] A. M. Zurita, I. Corbella, M. Martín-Neira, M. A. Plaza, F. Torres, and F. J. Benito, "Towards a smos operational mission: Smosops-hexagonal," *IEEE Journal of Selected Topics in Applied Earth Observations and Remote Sensing*, vol. 6, no. 3, pp. 1769–1780, 2013.

[20] F. Aurenhammer, "Voronoi diagrams—a survey of a fundamental geometric data structure," *ACM Comput. Surv.*, vol. 23, no. 3, p. 345–405, Sep. 1991. [Online]. Available: https://doi.org/10.1145/116873.116880

[21] A. Camps, M. Vall-llossera, I. Corbella, F. Torres, and N. Duffo, "Angular and radiometric resolution of y-shaped nonuniform synthetic aperture radiometers for earth observation," *IEEE Geoscience and Remote Sensing Letters*, vol. 5, no. 4, pp. 793–795, 2008.

[22] L. Jyh-Miin and Mezmay, "PyNUFFT: Python non-uniform fast Fourier transform," commit: 1c907a3. [Online]. Available: https://github.com/pynufft/pynufft